minerals

MDPI

Article

Petrogenesis and Tectonic Implication of the Hongtaiping High-Mg Diorite in the Wangqing Area, NE China: Constraints from Geochronology, Geochemistry and Hf Isotopes

Siyu Lu [1], Yunsheng Ren [1,2,*], Qun Yang [1], Yujie Hao [1,3] and Xuan Zhao [4]

[1] College of Earth Sciences, Jilin University, Changchun 130061, China
[2] Institute of Disaster Prevention, Langfang 065201, China
[3] Key Laboratory of Mineral Resources Evaluation in Northeast Asia, Ministry of Natural Resources, Changchun 130026, China
[4] Jiangxi Earthquake Agency, Nanchang 330026, China
* Correspondence: renys@jlu.edu.cn

Abstract: This study presents new data from zircon U–Pb dating and Hf isotope analysis, as well as whole-rock major- and trace-element compositions of the Hongtaiping high-Mg diorite in the Wangqing area of Yanbian, NE China. Laser ablation inductively coupled plasma mass spectrometry (LA–ICP–MS) zircon U–Pb dating gives an eruption age of ca. 267 Ma for the high-Mg diorite. These samples have MgO contents of 13.30% to 16.58% and high transition metal element concentrations, classified as sanukite. Their rare earth element (REE) contents range from 45.2 to 68.4 ppm and are characterized by slightly positive Eu anomalies (Eu/Eu* = 1.08–1.17). They show enrichment in light REEs (LREEs) and depletion in heavy REEs (HREEs), with LREE/HREE ratios = 6.54–6.97 and $(La/Yb)_N$ values = 7.24–8.08. The Hongtaiping high-Mg diorite is enriched in Rb, U, K, and Sr, but depleted in Th, Nb, and Ta. High MgO contents, $Mg^{\#}$ values, and transition metal element concentrations imply that the magma experienced insignificant crystallization fractionation and crustal contamination. Relatively homogenous positive Hf isotopic values indicate that the original magma was generated by the partial melting of a depleted mantle wedge that was metasomatized by subducting slab fluids. The magma was generated by the moderate degree partial melting (20%–30%) of a garnet lherzolite source. Combined with previous studies, this shows that the high-Mg diorite was formed by the northward subduction of the Paleo-Asian oceanic plate during the Middle Permian.

Keywords: high-Mg diorite; geochronology; geochemistry; Hf isotope; Paleo-Asian Ocean

check for updates

Citation: Lu, S.; Ren, Y.; Yang, Q.; Hao, Y.; Zhao, X. Petrogenesis and Tectonic Implication of the Hongtaiping High-Mg Diorite in the Wangqing Area, NE China: Constraints from Geochronology, Geochemistry and Hf Isotopes. *Minerals* **2022**, *12*, 1002. https://doi.org/10.3390/min12081002

Academic Editors: Sergei Khromykh and Andrei Tsygankov

Received: 27 June 2022
Accepted: 3 August 2022
Published: 8 August 2022

1. Introduction

As an important method for studying the time limitation of plate subduction, the tectonic setting of the subduction zone, and the tectonic evolution of the orogenic belt, high-magnesium andesite (HMA) is one of the hotspots of geoscience research [1–8]. HMA refers to those andesites characterized by higher MgO, lower TFeO/MgO, Al_2O_3, and CaO contents than typical island arc andesite [8]. Presently, it is divided into four main types: boninite, bajaite, adakitic HMA, and sanukite. Boninite is a volcanic rock that has a high magnesium content and is rich in fluid and saturated with silica [9,10]. High SiO_2 (>52%) and MgO (>8%) contents, and low TiO_2 (<0.5%) contents, are its key geochemical characteristics [11]. Bajaite is a suite of magnesian andesite and basalt, and basaltic andesite [4,5], which is characterized by high Sr (506–3800 ppm) and Ba (280–2300 ppm) concentrations, and high Sr/Y ratios [7]. Adakitic HMA has higher MgO, $Mg^{\#}$, Cr, and Ni concentrations than adakite. Sanukite has the characteristics of a high MgO content, high Cr and Ni concentrations, and enrichment in large-ion lithophile elements (LILEs) [6]. Sanukite includes intrusive and volcanic rocks with the above sanukitic geochemical features [12].

Presently, several issues in NE China, especially the final closure time of the Paleo-Asian Ocean, are in debate. Most researchers suggest that the final closure happened between the Late Permian and Middle Triassic [13–19], but other researchers proposed that the Paleo-Asian Ocean closed during the Late Devonian and Early Carboniferous [20–22]. The Yanbian area, located in the eastern segment of the Central Asian Orogenic Belt (CAOB), experienced the superimposition and transformation of the Paleo-Asian Ocean and Paleo-Pacific Ocean domains, which resulted in multiple periods of magmatic and metallogenic events [23,24], as well as ideal conditions to solve these controversies. Previous studies mainly focused on the geochronology, geochemistry, and source area of felsic igneous rocks in this region [14,17,18,25–30]. Due to lesser exposure, relevant work on mafic rocks concentrated on the Wudaogou complex [31,32] and Qianshan intrusion [33–35]. Until now, only Li et al. [26] discovered high-Mg diorite in the Hunchun area and proposed that these rocks likely formed in the Middle Triassic from mantle peridotite by reacting with Si-rich melts, similar to the magmatic processes of sanukite. Thus, the data on high-Mg diorite presented in this paper can create diagnostic constraints for the tectonic evolution of the eastern Paleo-Asian Ocean.

This study presents new data on LA–ICP–MS zircon U–Pb dating, in situ Hf isotopic analysis, and whole-rock major- and trace-element analysis. Some key issues are discussed, including the emplacement age, petrogenesis, and tectonic setting of the high-Mg diorite. The data and discussions provide new evidence for the tectonic evolution of the Yanbian area.

2. Geological Setting and Sample Descriptions

The CAOB (Figure 1a) is one of the largest and most complex orogens in the world [36–39]. The eastern segment of the CAOB (accepted as the Xing'an–Mongolia Orogenic Belt, XMOB) is composed of a series of microblocks and orogens consisting of Phanerozoic island arc and accretionary/collisional complex, and it experienced the reformation of the Paleo-Asian Ocean, the Mongo-Okhotsk Ocean, and the Paleo-Pacific Ocean regimes during the Paleozoic to Mesozoic [13,15–17,19,38–42]. Microblocks mainly consist of, from northwest to southeast, the Erguna, Xing'an, Songnen-Zhangguangcai Range, Jiamusi, and Khanka massifs (Figure 1b). Orogens include the Duobaoshan island arc belt and the continental margin accretionary belt of the NCC [16,43]. The Yuejinshan Complex and Nadanhada Terrane to the east of the Jiamusi Massif developed during the Permian and Mesozoic [44,45].

The Yanbian area of NE China, bounded by the Dunhua–Mishan Fault to the northwest and the Gudonghe–Fuerhe Fault to the south [14,35,46], is located among the continental margin accretionary belt, Songnen–Zhangguangcai Range, and Jiamusi and Khanka massifs. Archean to early Proterozoic greenschist and amphibolite–facies metamorphic rocks are only distributed in the Helong area [14,35,46,47]. Paleozoic strata experiencing various degrees of metamorphism and deformation and Mesozoic–Cenozoic volcanics and sediments develop widely [13]. The voluminous Phanerozoic granitoids that make up the Yanbian area known as the "granite ocean" are associated with limited and scattered mafic intrusions (Figure 1c; Table 1), and constitute the magmatic rocks of this area. As found in a previous study, there were four periods of magmatism, namely the late Permian to Early Triassic (280–245 Ma), the Late Triassic (225–220 Ma), the Jurassic (200–150 Ma), and the Early Cretaceous (135–105 Ma) [23,48].

The Hongtaiping Cu polymetallic deposit, with a proven reserve of 6257 t Cu, 2472 t Pb, and 13,527 t Zn, is located in Wangqing County of the Yanbian area. Strata in the ore district are mainly composed of the Middle Permian Miaoling Formation felsic volcanic rocks, and sedimentary rocks with limestone intercalations [24,48]. Triassic and Jurassic felsic dikes were documented. Two mineralization types are identified at the Hongtaiping deposit, i.e., stratiform VMS-type mineralization (268.3 ± 2.6 Ma) [24] in the Miaoling Formation and quartz-sulfide vein-type mineralization (206.8 ± 9.0 Ma) [49] controlled by fractures.

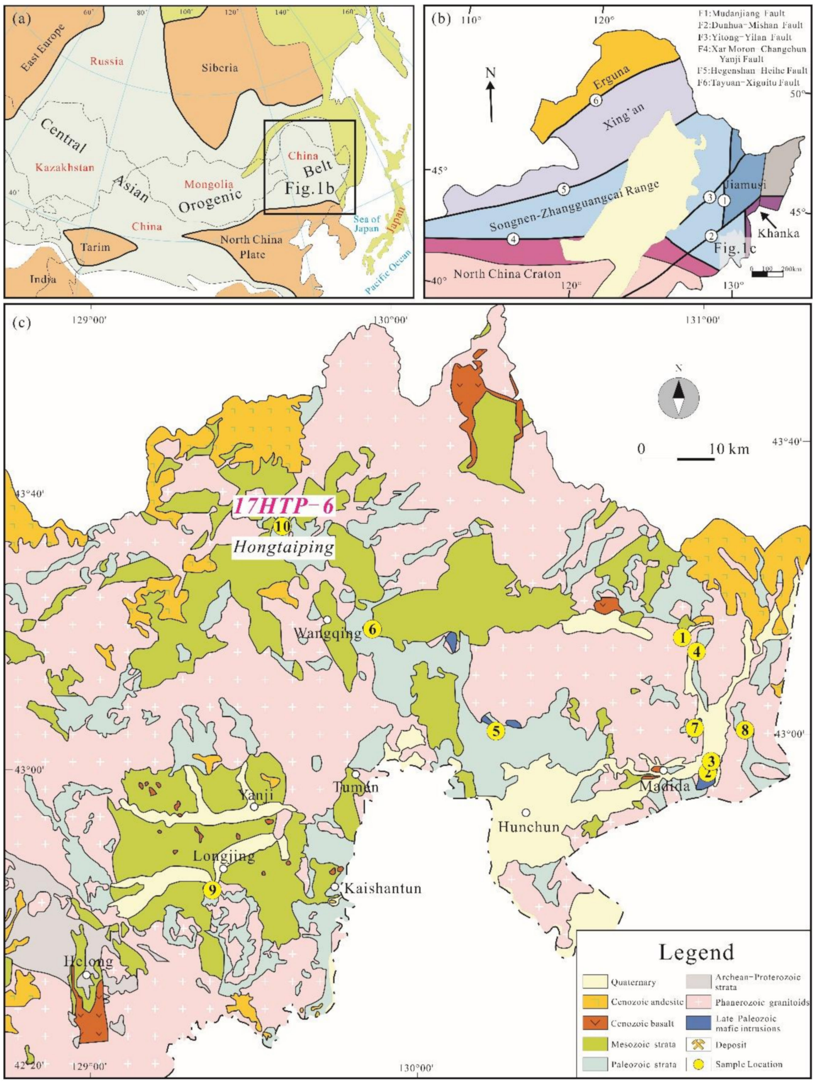

Figure 1. (**a**) Simplified tectonic map showing the location of the CAOB (modified from [36]); (**b**) tectonic divisions of NE China (modified from [43]); (**c**) simplified regional geologic map of the Yanbian area (modified from [35]).

Table 1. Permian and Early Triassic mafic intrusions in the Yanbian area.

Order	Sample	Latitude	Longitude	Pluton	Lithology	Age (Ma)	Method	Reference
1	JXNC-I-2			Wugaogou	Gabbro	270 ± 10	SHRIMP	[31]
2	YH8-1			Qianshan	Gabbro	282 ± 2	LA–ICP–MS	[34]
3	JXB-6A			Wudaogou	Gabbroic diorite	263.5 ± 5.1	LA–ICP–MS	[32]
4	06HCH-55	42°58′08″	130°55′25″	Qianshan	Gabbro	273 ± 2	SHRIMP	[33,35]
5	09HC-18	43°01′11″	130°58′25″	Shuguang	Diorite	257 ± 2	SHRIMP	[35]
6	09HC-26	43°40′11″	129°55′30″	Wangqing	Diorite	263 ± 3	LA–ICP–MS	[35]
7	09HC-12	43°01′09″	130°19′25″	Qinggoushan	Gabbro	254 ± 3	LA–ICP–MS	[38]
8	HC01	43.0148417°	131.000115°		Gabbro	266.9 ± 5.2	LA–ICP–MS	[50]
9	B4117	42°39′35″	129°29′57″	Zhixin	Hornblende gabbro	251 ± 1	LA–ICP–MS	[51]
10	17HTP-6	43°34′19″	129°33′21″	Hongtaiping	High-Mg diorite	267.0 ± 1	LA–ICP–MS	This study

Sample 17HTP-6, a high-Mg diorite (Figure 2a), was collected from the open pit of the Hongtaiping deposit (43°34′19″ N, 129°33′21″ E) for LA–ICP–MS zircon U–Pb dating and in situ Hf isotopic and whole-rock chemical analysis. The high-Mg diorite is grayish-white and displays an idiomorphic–hypidiomorphic granular texture and massive structure (Figure 2a). It consists of hornblende (~55%), plagioclase (~40%), and minor alkali feldspar and quartz (~5%) (Figure 2b,c).

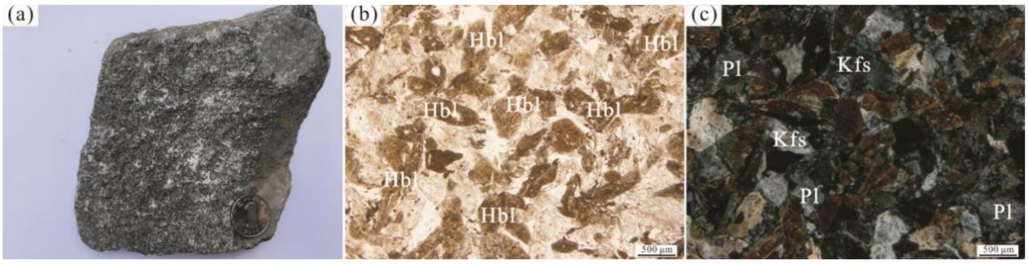

Figure 2. (**a**) High-Mg diorite; (**b**) high-Mg diorite (plane polar); (**c**) high-Mg diorite (crossed polar).

3. Analytical Methods

3.1. Zircon U–Pb Geochronology

Zircon grains were separated through a combination of magnetic and heavy liquid separation techniques and were handpicked under a binocular microscope at the Beijing Geoanalysis Co., Ltd. (Beijing, China). The handpicked zircons were mounted in epoxy resin and polished to about half their thickness. All zircon grains were photographed in transmitted and reflected light, as well as imaged with cathodoluminescence (CL).

LA–ICP–MS zircon U–Pb dating was carried out at the Key Laboratory of Mineral Resources Evaluation in Northeast Asia, Ministry of Natural Resources, Jilin University, Changchun, China, using an Agilent 7500a inductively coupled plasma mass spectrometer (ICP-MS) equipped with a 193-nm ArF Excimer laser system (LA). The standard zircon, 91500 [52], was used as an external standard to normalize isotopic fractionation during analysis. The analytical details were described by Hao et al. [53].

3.2. Whole-Rock Major and Trace Element Analysis

Five samples were collected for whole-rock chemical analysis. The fresh and unaltered samples were crushed, cleaned with deionized water, and ground to a 200 mesh using an agate mill. Major and trace element analyses were performed at the State Key Laboratory of Ore Deposit Geochemistry, Institute of Geochemistry, Chinese Academy of Sciences (IGCAS), Guiyang, China, using Thermo Fisher ARL Perform' X 4200 X-ray fluorescence spectrometer (XRF) and PlasmaQuant MS Elite ICP–MS, respectively. The analytical details were described by Qi and Zhou [54]. The analytical results for the major elements had a precision of <5%, as determined using GSR-1 and GSR-3 Chinese national standards, and a precision of <10% for the trace elements using international OU-6 and GBPG-1 standards. The detection limit for the trace element is better than 0.5 ppb, and triplicate analyses were reproducible within 5% for all the elements.

3.3. In Situ Zircon Hf Isotope Analysis

In situ zircon Hf isotope analysis was conducted on the same zircon grains previously subjected to U–Pb isotopic analyses, using a Thermo Neptune-Plus multicollector (MC–ICP–MS) equipped with a Geolas Pro 193-nm ArF excimer laser ablation (LA) system at the Beijing Geoanalysis Co., Ltd. All data were acquired on zircon in single-spot ablation mode with a spot size of 44 μm. The standard zircon GJ-1 [55] was used as a reference material. The detailed analytical procedures were described by Wu et al. [56]. The present-day chondritic ratios of ^{176}Hf/^{177}Hf = 0.282772 and ^{176}Lu/^{177}Hf = 0.0332 [57] were adopted to calculate the εHf(t) values. Hf model ages were calculated as described in Nowell et al. [58], Amelin et al. [59], and Griffin et al. [60].

4. Results

4.1. Internal Structure and Texture of Zircon

The CL images of representative zircons are presented in Figure 3. Zircons mainly have a length of 40–80 μm and a width of 30–60 μm, with aspect ratios of 1:1–2:1. The rims comprise thin overgrowths, are CL-dark, and exhibit faint, poorly developed oscillatory zoning. The core domains are relatively large and bright, and seldom have microfractures or cracks but have abundant micro-inclusions [61].

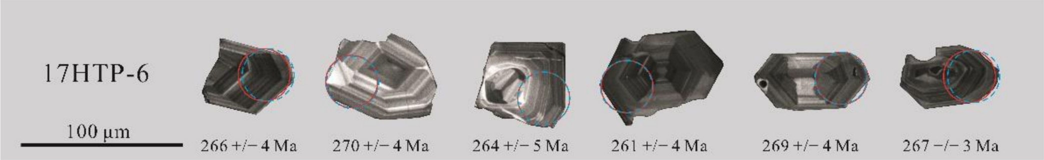

Figure 3. Representative zircon CL images of the high-Mg diorite. Red circles represent the analytical spots of LA–ICP–MS U–Pb analyses, and blue circles represent the analytical spots of Lu–Hf analyses. The U–Pb and Lu–Hf analytical diameters are 32 μm.

4.2. Zircon U–Pb Dating

The LA–ICP–MS zircon U–Pb dating results of sample 17HTP-6 are presented in Table 2, and zircon U–Pb concordia diagrams are shown in Figure 4. Fourteen analytical spots produced $^{206}Pb/^{238}U$ ages of 276–261 Ma (Figure 4a) and yielded a weighted mean $^{206}Pb/^{238}U$ age of 267.0 ± 2.8 Ma (MSWD = 1.7, *n* = 14, Figure 4b). Two older ages (405 Ma and 315 Ma) are interpreted to be the crystallization ages of inherited or captured zircons entrained by the magma.

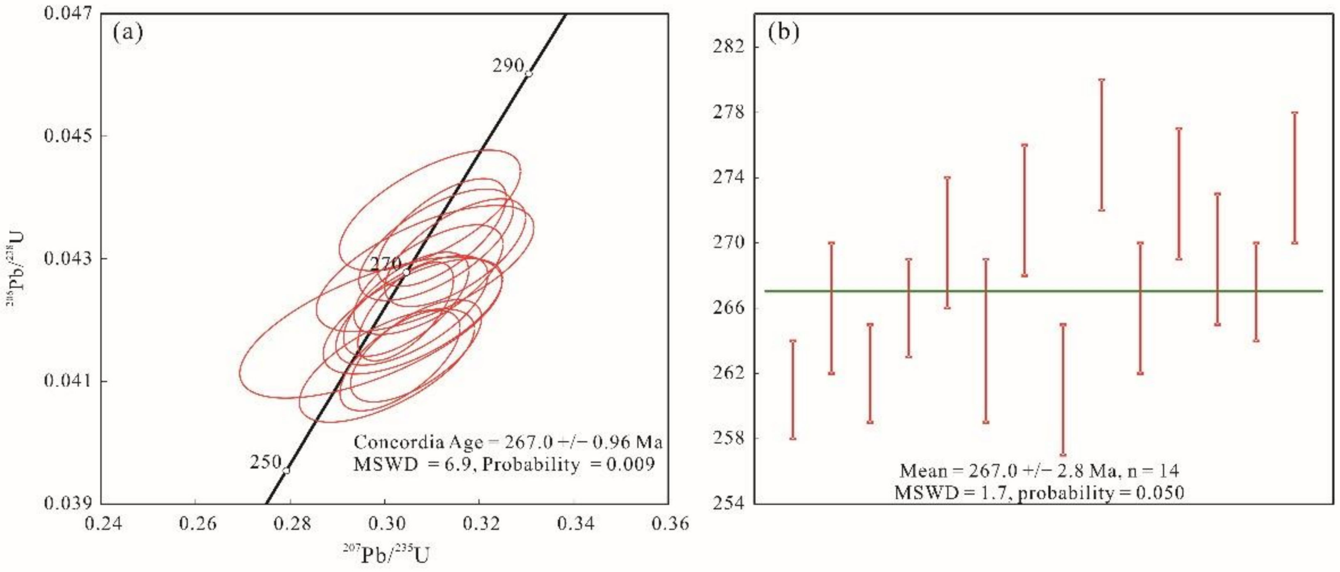

Figure 4. LA–ICP–MS zircon U–Pb diagrams of the high-Mg diorite. (**a**) Diagram of the concordia age; (**b**) Diagram of the weighted mean age.

Table 2. LA–ICP–MS zircon U–Pb dating results of the high-Mg diorite.

Sample No.	**Th (ppm)**	**U (ppm)**	**Th/U**	**Isotopic Ratios**						**Rho**	**Ages (Ma)**						**D%**
				$^{207}Pb/^{206}Pb$		**$^{207}Pb/^{235}U$**		**$^{206}Pb/^{238}U$**			**$^{207}Pb/^{206}Pb$**		**$^{207}Pb/^{235}U$**		**$^{206}Pb/^{238}U$**		
				Ratio	**1σ**	**Ratio**	**1σ**	**Ratio**	**1σ**		**Ages**	**1σ**	**Ages**	**1σ**	**Ages**	**1σ**	
91500	25.43	73.44	0.35	0.07298	0.00203	1.80552	0.0503	0.17949	0.00247		1013.5	55.32	1047.5	18.21	1064.2	13.51	
17HTP-6-1	731.41	490.78	1.49	0.05321	0.00146	0.30323	0.00838	0.04134	0.00054	0.30	338	39	269	7	261	3	−23.2
17HTP-6-2	247.62	339.2	0.73	0.05261	0.00184	0.30577	0.01061	0.04216	0.00059	0.31	312	53	271	8	266	4	−15
17HTP-6-3	588.6	433.1	1.36	0.0536	0.0016	0.30664	0.00915	0.0415	0.00055	0.31	354	43	272	7	262	3	−26.6
17HTP-6-4	963.01	1048.82	0.92	0.05241	0.00112	0.30445	0.00668	0.04214	0.00053	0.30	303	28	270	5	266	3	−12.6
17HTP-6-5	121.86	166.11	0.73	0.05225	0.00261	0.30856	0.0152	0.04284	0.00068	0.31	296	83	273	12	270	4	−9
91500	25.04	72.54	0.35	0.07711	0.00185	1.90225	0.04605	0.17895	0.00238		1124.1	46.98	1081.9	16.11	1061.2	13.02	
17HTP-6-7	584.77	466.38	1.25	0.05146	0.00323	0.29709	0.01832	0.04188	0.00076	0.30	261	108	264	14	264	5	1.1
17HTP-6-8	376.44	438.1	0.86	0.053	0.00166	0.31493	0.00983	0.0431	0.00058	0.31	329	46	278	8	272	4	−17.6
17HTP-6-9	709.47	978.6	0.72	0.05459	0.00087	0.48771	0.00823	0.0648	0.00078	0.49	395	18	403	6	405	5	2.4
17HTP-6-10	216.3	460.32	0.47	0.05283	0.00217	0.30047	0.01223	0.04126	0.00061	0.30	322	65	267	10	261	4	−19.3
91500	25.28	73.51	0.34	0.07409	0.00178	1.83155	0.04457	0.17932	0.00238		1043.8	47.74	1056.8	15.98	1063.2	13.03	
17HTP-6-12	155.87	278.2	0.56	0.05127	0.00212	0.30959	0.01266	0.04379	0.00065	0.31	253	67	274	10	276	4	9.4
17HTP-6-14	255.06	234.78	1.09	0.05276	0.00218	0.30596	0.01253	0.04206	0.00062	0.31	318	66	271	10	266	4	−17
17HTP-6-15	223.78	234.2	0.96	0.05216	0.00182	0.3109	0.01079	0.04323	0.0006	0.31	292	54	275	8	273	4	−6.8
91500	26.50	76.28	0.35	0.07477	0.00212	1.84462	0.05233	0.17891	0.00251		1062.4	55.92	1061.5	18.68	1061	13.72	
17HTP-6-16	155.47	314.83	0.49	0.05257	0.00177	0.30928	0.0104	0.04266	0.00059	0.31	310	51	274	8	269	4	−13.5
17HTP-6-17	812.69	1143.95	0.71	0.05409	0.00195	0.37363	0.0134	0.05009	0.00071	0.37	375	55	322	10	315	4	−16.3
17HTP-6-18	256.49	316.65	0.81	0.05226	0.00149	0.30454	0.00874	0.04226	0.00056	0.30	297	41	270	7	267	3	−10.3
17HTP-6-20	314.09	291.06	1.08	0.05211	0.0015	0.31206	0.009	0.04343	0.00058	0.31	290	42	276	7	274	4	−5.7
91500	24.56	71.58	0.34	0.07477	0.00187	1.84903	0.0468	0.17932	0.00242		1062.3	49.56	1063.1	16.68	1063.3	13.24	

4.3. Major and Trace Element Compositions

Whole-rock major- and trace-element compositions are listed in Table 3. The Hongtaiping high-Mg diorite samples contained SiO_2 = 43.96%–46.57%, Al_2O_3 = 13.34%–14.72%, total Fe_2O_3 = 10.05%–11.37%, MgO = 13.30%–16.58%, and (Na_2O + K_2O) = 1.80%–3.22%. The samples contained rare earth elements (REEs) = 45.2–68.4 ppm and were characterized by slightly positive Eu anomalies (Eu/Eu* = 1.08–1.17; Figure 5a). They show enrichment of light REEs (LREEs) and depletion of heavy REEs (HREEs), with LREE/HREE ratios = 6.54–6.97, and $(La/Yb)_N$ values = 7.24–8.08. On the primitive mantle (PM)-normalized trace element diagram (Figure 5b), these samples are enriched in Rb, U, K, and Sr and depleted in Th, Nb, and Ta. The high-Mg diorite samples are classified as andesite and basalt series on a Zr/TiO_2*0.0001 vs. Nb/Y diagram (Figure 6a) and as calc-alkaline series on a Th vs. Co diagram (Figure 6b).

Table 3. Whole-rock major (wt.%) and trace (ppm) element compositions of the high-Mg diorite.

Sample	17HTP-6-1	17HTP-6-2	17HTP-6-3	17HTP-6-4	17HTP-6-5	OU-6	GBPG-1
Major elements (wt.%)							
SiO_2	43.96	45.19	46.57	45.13	45.62		
Al_2O_3	13.34	13.57	14.72	13.42	13.78		
Fe_2O_3t	11.37	11.02	10.05	11.07	10.65		
MgO	16.58	16.03	13.30	15.68	15.08		
CaO	6.29	6.09	6.47	6.28	6.12		
Na_2O	1.37	1.53	2.31	1.71	1.80		
K_2O	0.43	0.48	0.91	0.50	0.61		
MnO	0.25	0.22	0.19	0.17	0.22		
P_2O_5	0.23	0.22	0.25	0.22	0.23		
TiO_2	0.95	0.90	1.04	0.96	0.95		
LOI	5.14	4.93	4.04	4.78	4.76		
Total	99.90	100.19	99.84	99.92	99.81		
Trace elements (ppm)							
Li	99.7	91.2	77.2	80.9	86.9	95.2	20.1
Be	0.85	0.83	1.03	0.84	0.87	2.72	0.82
Sc	18.7	17.8	20.7	18.7	18.5	22.2	15.4
V	189	183	211	199	193	127	98.1
Cr	1326	1186	916	1226	1095	71.8	179
Co	63.4	59.5	53.3	61.8	56.2	29.4	21.0
Ni	562	506	351	486	464	38.0	57.0
Cu	10.5	11.7	13.3	15.8	11.3	45.0	27.4
Zn	138	115	105	102	110	107	83.7
Ga	17.8	16.7	18.4	17.1	17.1	23.8	19.4
As	335	219	166	82.1	210	13.0	1.26
Rb	18.7	17.7	44.8	21.5	23.9	124	60.9
Sr	366	402	542	391	459	139	360
Y	11.9	11.7	13.7	12.7	12.3	28.5	19.1
Zr	70.9	71.3	79.8	71.1	73.8	174	235
Nb	2.29	2.29	2.64	2.32	2.41	14.7	10.1
Mo	0.48	0.40	1.20	1.03	0.48	0.53	1.75
Ag	0.06	0.09	0.14	0.10	0.06	0.22	0.19
Cd	0.07	0.07	0.10	0.09	0.06	0.1	0.09
Sn	0.80	0.60	0.75	0.69	0.74	2.57	0.58
Sb	4.26	3.73	2.88	2.92	3.63	0.53	0.06

Table 3. *Cont.*

Sample	17HTP-6-1	17HTP-6-2	17HTP-6-3	17HTP-6-4	17HTP-6-5	OU-6	GBPG-1
Cs	2.78	2.19	5.03	3.14	2.66	7.68	0.31
Ba	66.1	77.8	182	88.3	106	495	894
La	9.83	9.52	11.6	9.57	10.3	32.0	48.6
Ce	22.7	22.0	26.1	22.3	23.2	70.5	91.2
Pr	2.66	2.59	3.03	2.67	2.72	7.91	11.1
Nd	12.1	11.9	13.9	12.3	12.5	30.5	41.1
Sm	2.66	2.57	2.99	2.70	2.67	5.97	6.39
Eu	0.92	0.91	1.11	0.93	0.94	1.41	1.85
Gd	2.44	2.38	2.81	2.55	2.52	5.27	4.69
Tb	0.34	0.33	0.39	0.36	0.35	0.81	0.59
Dy	1.98	1.93	2.26	2.10	2.02	4.93	3.08
Ho	0.39	0.38	0.44	0.41	0.40	1.01	0.65
Er	1.04	1.01	1.18	1.07	1.06	2.86	1.95
Tm	0.14	0.14	0.16	0.15	0.14	0.43	0.29
Yb	0.91	0.89	1.03	0.95	0.93	2.89	1.96
Lu	0.14	0.13	0.15	0.14	0.14	0.44	0.30
Hf	1.71	1.64	1.92	1.71	1.75	4.73	5.80
Ta	0.13	0.13	0.15	0.13	0.14	1.04	0.40
W	0.23	0.95	0.33	0.15	0.21	1.11	0.16
Tl	0.16	0.13	0.32	0.17	0.17	0.52	0.28
Pb	2.53	2.45	4.18	3.02	2.05	29.3	13.9
Bi	0.09	0.06	0.06	0.06	0.05	0.27	0.01
Th	0.58	0.58	0.68	0.57	0.64	11.5	11.5
U	0.58	0.41	0.35	0.39	0.42	1.97	0.89

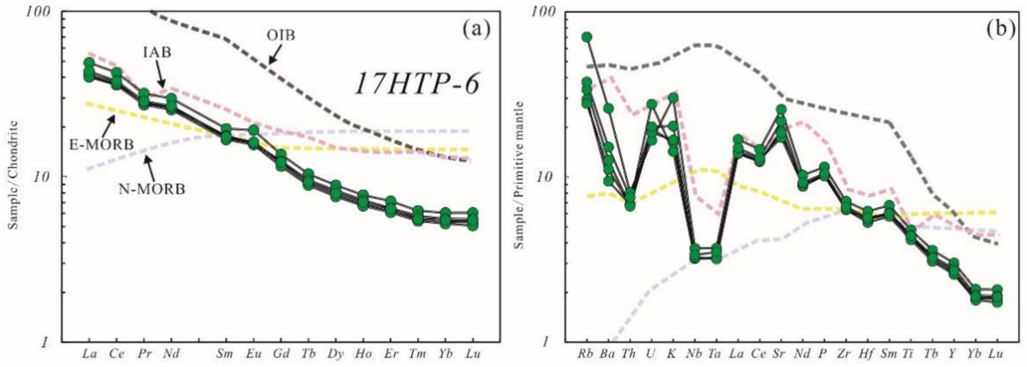

Figure 5. (**a**) Chondrite-normalized REE diagrams; (**b**) PM-normalized trace element diagrams for the high-Mg diorite. The C1 chondrite-normalized, PM-normalized, OIB, E-MORB, and N-MORB values are from [62]. The IAB values are from [63].

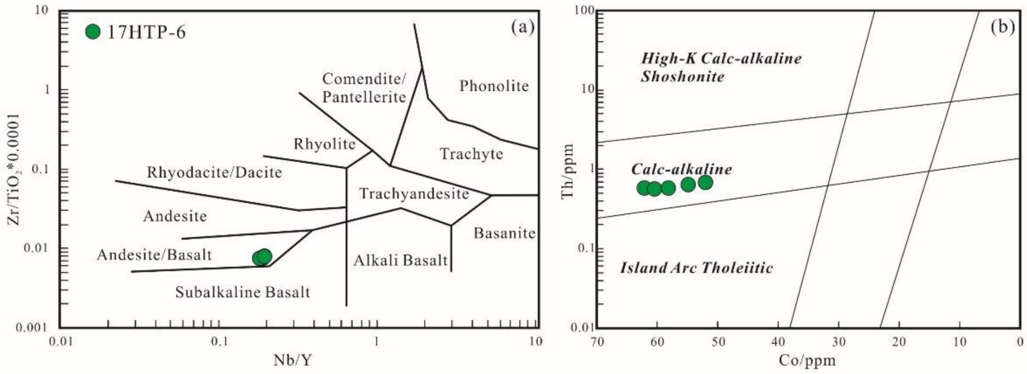

Figure 6. (**a**) Zr/TiO_2*0.0001 vs. Nb/Y diagram (modified from [64]); (**b**) Th vs. Co diagram (modified from [65]).

4.4. In Situ Zircon Hf Isotopic Compositions

In situ zircon Hf isotopic compositions are listed in Table 4. Zircon grains in the high-Mg diorite have initial $^{176}Hf/^{177}Hf$ ratios of 0.282764–0.282950, with $\varepsilon_{Hf}(t)$ values and T_{DM2} ages ranging from 6.7 to 12.2 (Figure 7) and 929 to 511 Ma, respectively.

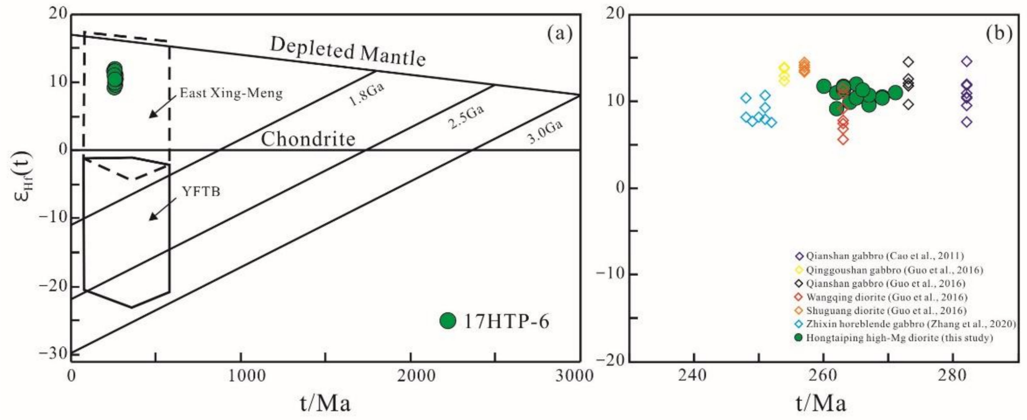

Figure 7. (**a**) $\varepsilon_{Hf}(t)$ vs. t(Ma) diagram for zircons from the high-Mg diorite. Xing-Meng = XMOB; YFTB = Yanshan Fold and Thrust Belt (Ranges of XMOB and YFTB are from Yang et al. [66]); (**b**) detailed distribution of samples in $\varepsilon_{Hf}(t)$ vs. T(Ma) diagram enlarged from the square area in (**a**). The isotopic data are from [34,35,51].

Table 4. In situ zircon Hf isotopic compositions of the high-Mg diorite.

Sample	^{176}Yb/^{177}Hf	2σ	^{176}Lu/^{177}Hf	2σ	^{176}Hf/^{177}Hf	2σ	Hf$_i$	$\varepsilon_{Hf}(0)$	$\varepsilon_{Hf}(t)$	T$_{DM}$ (Ma)	T$_{2DM}$ (Ma)	f$_{Lu/Hf}$	t(Ma)
17HTP-6-1	0.037124	0.000478	0.001574	0.000022	0.282907	0.000017	0.282900	4.8	10.3	496	630	−0.95	261
17HTP-6-2	0.041057	0.000420	0.001714	0.000015	0.282893	0.000035	0.282884	4.3	9.8	519	663	−0.95	266
17HTP-6-3	0.090221	0.000406	0.003196	0.000024	0.282813	0.000023	0.282798	1.5	6.7	660	860	−0.90	262
17HTP-6-4	0.124537	0.001427	0.004711	0.000026	0.282851	0.000023	0.282827	2.8	7.9	631	788	−0.86	270
17HTP-6-5	0.027130	0.000650	0.000996	0.000023	0.282875	0.000014	0.282870	3.6	9.3	535	696	−0.97	264
17HTP-6-6	0.024001	0.000850	0.000855	0.000031	0.282844	0.000017	0.282840	2.5	8.4	576	759	−0.97	272
17HTP-6-7	0.110644	0.001535	0.004020	0.000040	0.282878	0.000020	0.282858	3.7	8.8	577	724	−0.88	261
17HTP-6-8	0.028720	0.000445	0.001058	0.000019	0.282866	0.000017	0.282861	3.3	9.2	547	708	−0.97	276
17HTP-6-9	0.144028	0.000886	0.004936	0.000015	0.282869	0.000022	0.282845	3.4	8.4	606	751	−0.85	266
17HTP-6-10	0.071030	0.000655	0.002667	0.000033	0.282912	0.000022	0.282898	4.9	10.5	505	627	−0.92	273
17HTP-6-11	0.035574	0.000840	0.001289	0.000033	0.282957	0.000016	0.282950	6.5	12.2	422	511	−0.96	269
17HTP-6-12	0.083950	0.001669	0.003028	0.000054	0.282873	0.000018	0.282858	3.6	8.9	568	722	−0.91	267
17HTP-6-13	0.049584	0.000355	0.001858	0.000015	0.282773	0.000018	0.282764	0.0	5.7	695	929	−0.94	274
GJ-1-1	0.006831	0.000010	0.000295	0.000000	0.282015	0.000021							
GJ-1-2	0.006855	0.000013	0.000296	0.000000	0.281971	0.000019							
GJ-1-3	0.006849	0.000008	0.000296	0.000000	0.282006	0.000020							
GJ-1-4	0.006785	0.000013	0.000296	0.000000	0.282015	0.000022							

5. Discussion

5.1. Emplacement Age of the High-Mg Diorite and Middle Permian Magmatic Event in the Yanbian Area

In this study, zircon grains from the Hongtaiping high-Mg diorite exhibit typical oscillatory growth zoning, with high Th/U ratios (0.47–1.49), indicating their igneous origin [67,68]. The weighted mean ^{206}Pb/^{238}U age of 267.0 ± 2.8 Ma (n = 14) shows that this mafic intrusion emplaced in the Middle Permian. In the Yanbian area, as a result of the continuous subduction of the Paleo-Asian Ocean, the Permian was a notable magmatic activities period [14,17]. Previous studies have proved that the Early and Late Permian are two major stages of magmatism [14,17,18,25,26,34,35,69], whereas a large amount of Middle Permian has been reported. Lithologically, these are dominated by intermediate-felsic compositions with minor mafic intrusions. From east to west in the Yanbian area, the quartz diorite and granodiorite from the Wudaogou Group and gabbro in the Hunchun area have a formation age of 270 to 263 Ma [31,32,70]. Wu et al. [17] and Hou et al. [29] reported Hongshitun monzogranite (266 Ma) and two pyroclastic rocks (271–268 Ma) in the Wangqing area. A series of diorite–granodiorite (271–262 Ma) in the Tianbaoshan ore district has been identified by Ju [71], Sun et al. [72], Yang et al. [73,74], and Zhang et al. [75]. Liukesong gabbro (262 Ma) and granodiorite (263 Ma), and Xiaobutun quartz diorite (260 Ma) in the Dunhua area, have been reported by Liu et al. [27] and Wu et al. [17]. Moreover, Tang et al. [30] reported the monzogranite (265 Ma) in the Helong area in the southern Yanbian. Combined with these dating results, it has been suggested that the Middle Permian was also an important magmatism period in the Yanbian area.

5.2. Petrogenesis of the High-Mg Diorite

5.2.1. Alteration Effects

The Hongtaiping high-Mg diorite samples exhibit relatively high LOI values (4.04%–5.14%). The effects of alteration must be determined before their petrogenesis can be considered. High field-strength elements (HFSEs: e.g., Zr, Y, Nb, Th, and Ti) and transition elements (e.g., Cr, Ni, and Sc) are generally immobile during alteration and weathering [76]. Therefore, only immobile elements were used for the investigation of petrogenesis and tectonic setting of the high-Mg diorite.

5.2.2. Fraction Crystallization

Limited variations of geochemical compositions and high MgO contents, Mg$^{\#}$ values, and transition metal element concentrations suggest that the high-Mg diorite resulted from a very low-degree fractional magma [77]. The positive correlations between MgO and Fe_2O_3t suggest that ferromagnesian minerals such as olivine and clinopyroxene are major fractionating phases [35], whereas the negative correlations between MgO and SiO_2, Al_2O_3, CaO, Na_2O, K_2O, P_2O_5, and TiO_2 (Figure 8) demonstrate that Ti-bearing minerals, apatite, and plagioclase are not major fractional phases.

5.2.3. Crustal Contamination

Mantle-derived magma experiences crustal contamination during ascent [78]. Negative Nb–Ta anomalies indicate that the magma experienced crustal contamination. However, no significantly positive Zr–Hf anomalies exist, indicating that crustal contamination is not a major mechanism. Lu/Yb (0.15) and Nb/Ta (16.74–17.71) ratios are consistent with mantle-derived magmas (0.14–0.15 and 17.8, respectively) [60], rather than crustal-derived magmas (0.16–0.18 and 11.4, respectively) [79,80]. Low SiO_2 contents and high MgO contents, $Mg^{\#}$ values, and transition metal element concentrations, combined with homogeneous positive Hf isotopic values, imply that crustal contamination could not play a significant role during the magmatic evolution.

5.2.4. Nature of the Mantle Source

The high-Mg diorite samples in this study have lower SiO_2 (43.96%–46.57%) and higher TiO_2 contents (0.90%–1.04%) than boninite, lower SiO_2 content and Sr concentrations (366–542 ppm) than adakitic HMA, and lower Sr and Ba (66.1–182 ppm) concentrations than bajaite. Due to the relative enrichment in LREEs and LILEs, and the depletion of HREEs, $Mg^{\#}$ = 72%–74%, MgO content = 13.30%–16.58%, and Cr and Ni concentrations = 916–1326 ppm and 351–562 ppm, these samples fall into the sanukite area on the classification diagram of HMA (Figure 9a,b). Such geochemical features are distinctly different from crustal-derived rocks [79], together with relatively homogenous positive Hf isotopic values (6.7–12.2), indicating that the primary magma could be derived from the depleted mantle. Their high La/Nb (4.13–4.39) and La/Ta (71.58–76.32) ratios indicate that they were sourced from the lithospheric mantle ($La/Nb > 1$, $La/Ta > 20$) rather than the asthenospheric mantle ($La/Nb < 1$, $La/Ta \approx 10$) [81,82]. Negative Nb–Ta anomalies could also be caused by subduction-related fluid or melt metasomatism. The high-Mg diorite showed enrichment in LILEs and LREEs, and depletion in HFSEs and HREEs, consistent with rocks formed in subduction zones [83]. Large amounts of amphibole occurred in the samples, which shows that the original magma was water-rich [84], because amphibole and other water-bearing minerals crystallize only when water is saturated [85]. On the plots of Th/Yb vs. Ba/La and Th/Nb vs. Ba/Th diagrams (Figure 9c,d), there were constant Th/Yb and Th/Nb ratios and variable Ba/La and Ba/Th ratios, indicating a fluid-related enrichment. Thus, we propose that the magma was generated by the partial melting of a depleted mantle wedge that was metasomatized by subducting slab fluids.

Whole-rock REEs concentrations are mainly controlled by mantle composition and partial melting. Thus, the abundance and ratio of REEs can be widely used to define the characteristics of source area of mantle-derived rocks and the degree of mantle melting [86]. The Yb concentration in the initial melt during the melting of mantle peridotite was mainly controlled by residual garnet [87]. The melt formed by partial melting of mantle peridotite, accompanied by garnet residue, had a low Yb concentration and high LREE (such as La and Sm)/Yb ratios. However, the partial melting of spinel lherzolite will form a relatively flat melting trend, due to the fact distribution coefficients of La, Sm, and Yb in spinel are consistent [88]. A plot of Sm/Yb vs. Sm (Figure 10) indicates that the magmas were generated by moderate degree partial melting (20%–30%) of a garnet lherzolite source.

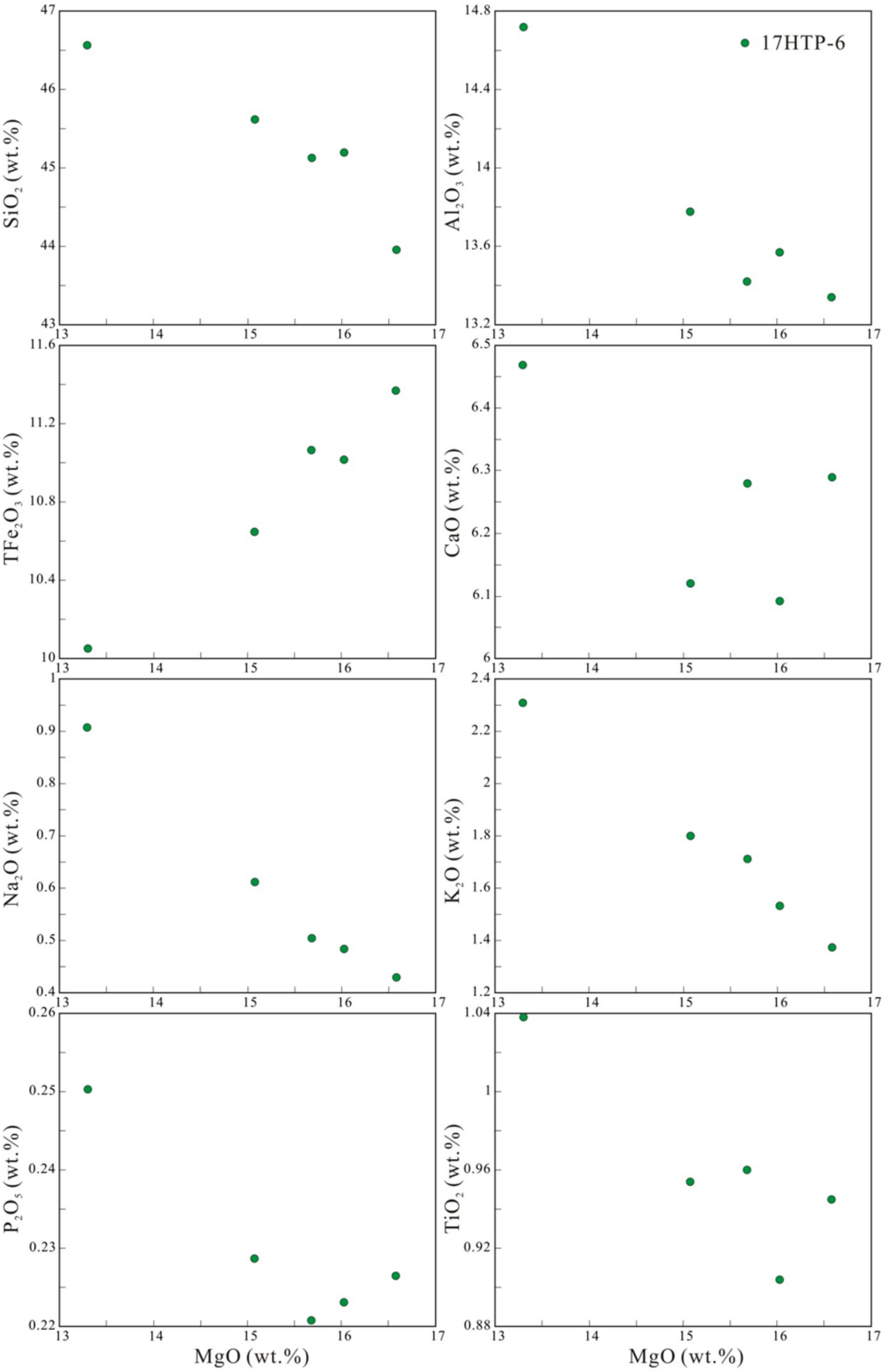

Figure 8. Harker diagrams of the high-Mg diorite.

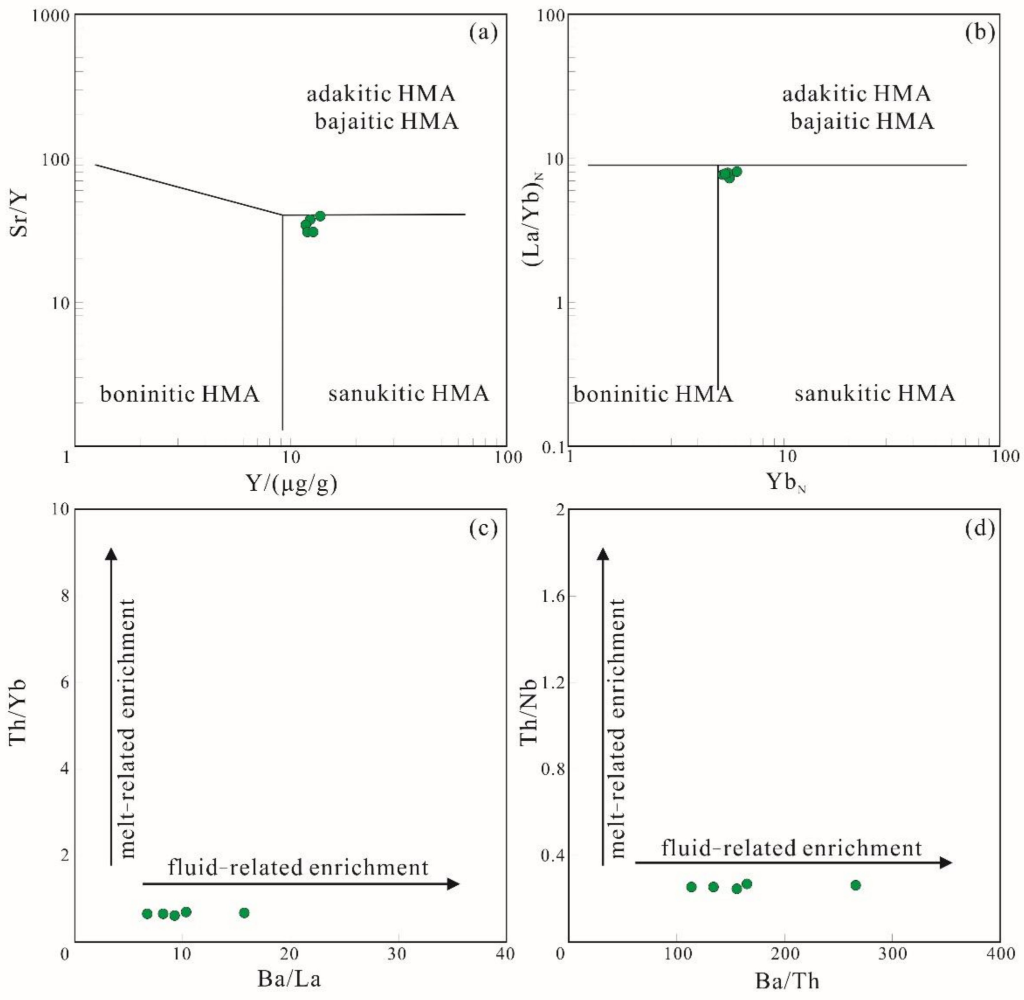

Figure 9. (**a**) Sr/Y vs. Y diagram and (**b**) $(La/Yb)_N$ vs. Yb_N diagram (modified after Kamei et al. [2]); (**c**) Th/Yb vs. Ba/La diagram (modified after Yang et al. [89]); (**d**) Th/Nb vs. Ba/Th diagram (modified after Hanyu et al. [90]).

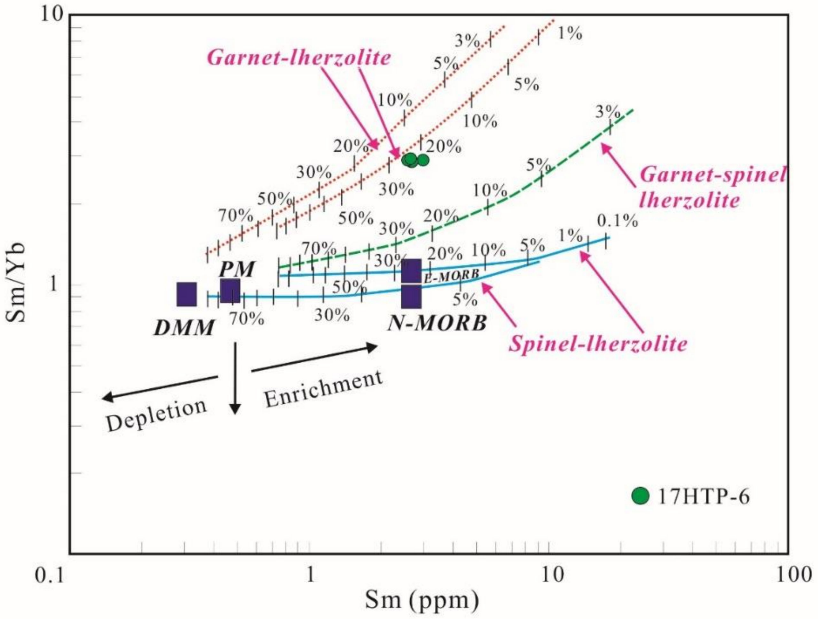

Figure 10. Sm/Yb vs. Sm diagram of the high-Mg diorite (modified after Feng et al. [86]).

5.3. Tectonic Implications

The Hongtaiping high-Mg diorite samples have similar Nb concentrations (2.29–2.64 ppm) to island-arc basalt (generally <2 ppm) [91], with enrichment in LILEs and LREEs, and depletion of HFSEs and HREEs, showing affinities of arc-type magmatism. On the plots of La/Yb vs. Sc/Ni and Th/Yb vs. Ta/Yb diagrams (Figure 11), the samples were mainly near the region of the continental arc, which reflects their arc-related nature. Geochemical features of Permian–Middle Triassic magmatic rocks in the Yanbian area reflect that they formed under the subduction of the Paleo-Asian oceanic plate [14,18,25,26,34]. Parental magmas of Wangqing diorites (263 Ma) were likely derived from the mantle wedge, metasomatized by sediment melt and fluid from the subducting Paleo-Asian oceanic plate [35]. Syn-collisional monzogranites (249–245 Ma) [14] represent the Early Triassic collision of the CAOB with the NCC and the final closure of the Paleo-Asian Ocean, which is also supported by an early Triassic bimodal igneous rock association in the Helong and Longjing areas (259–251 Ma) [50] and the middle Triassic high-Mg diorites in the Hunchun area (241–240 Ma) [26]. Thus, we propose that the Middle Permian Hongtaiping high-Mg diorite formed in the subducting environment of the Paleo-Asian oceanic plate.

In central Jilin, a large amount of research has indicated that the Paleo-Asian Ocean had not been closed before the early Triassic. Wu et al. [92] reported that the piemontite-bearing chert in the Paleozoic strata at Yantongshan formed in a continental-margin environment and probably marked the final closure in the terminal Paleozoic to initial Mesozoic. Seluohe high-Mg andesite (252 Ma) derived from the partial melting of the enriched mantle wedge induced by hydrous fluid from subducted sediments in a subduction zone [93]. Combined with the volcanic rock in the Daheshen Formation, Cao et al. [18] and Yu et al. [94] suggested that the rhyolite-dacite-tracydacite suite reflect an active continental margin setting. Volcanic rocks with an age of 256 to 253 Ma in the Daheishan horst imply that they may be related to the volcanic arcs formed by the subduction of the Paleo-Asian oceanic plate [95]. Rb–Sr mineral isochron data indicate that the metamorphism age of the Hulan Group, intruded by the syn-collisional Dayushan pluton (248 Ma) [15], occurred at ~250 Ma, reflecting that the final oceanic closure took place in the Late Permian to early Triassic [43].

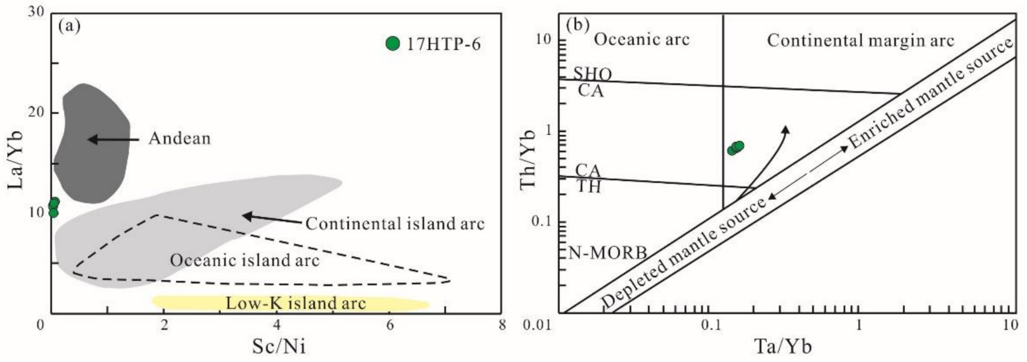

Figure 11. (**a**) La/Yb vs. Sc/Ni diagram (modified from [96]); (**b**) Th/Yb vs. Ta/Yb diagram (modified from [97]).

In the last decade, substantial data have supported the hypothesis that the Solonker–Xar Moron–Changchun–Yanji Suture (SXCYS) marks where the Paleo-Asian Ocean finally closed. A double-sided subduction model along the SXCYS has been established thanks to the following evidence: (1) the Late Permian–Middle Triassic high-Mg diorite or andesite are distributed along the SXCYS in both the southern combined NE China Blocks [26,98] and the northern NCC [93,99]; (2) igneous rock with arc affinities exists on both sides of the SXCYS [14,15,17,18,28–30,33–35,69,94,95,100]; (3) accretionary complexes related to subduction have been discovered in both the southern combined NE China Blocks and the northern NCC [25,93,99]. Liu et al. [19] gave a detailed discussion about the position of the eastern SXCYS and concluded that Changchun–Jilin–Dunhua–Yanji was the eastern extension of the SXCYS, as supported by paleontology, paleogeography, sediments and granitoid studies ([19] and references therein). As for the subduction polarity of the Hongtaiping high-Mg diorite, we propose that they formed under the northward subduction of the Paleo-Asian oceanic plate during the Middle Permian (Figure 12).

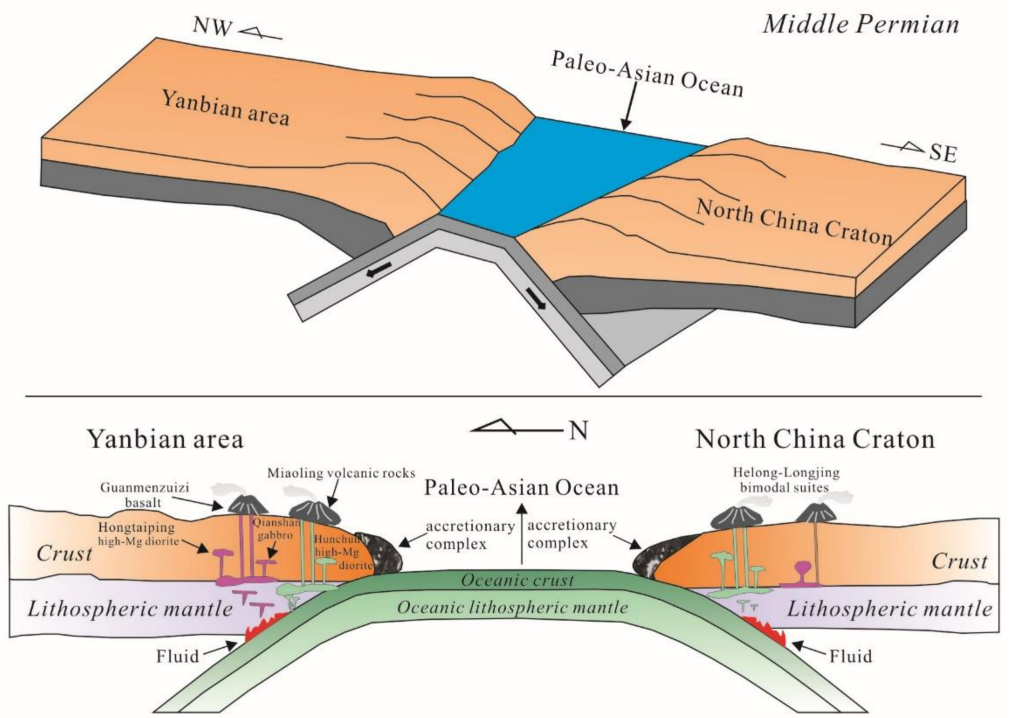

Figure 12. Simplified cartoon model that shows the Middle Permian–Early Triassic igneous rocks in the Yanbian area and the northern margin of the NCC (modified from [100]).

6. Conclusions

(1) New LA–ICP–MS zircon U–Pb dating results show that the high-Mg diorite was ca. 267 Ma.

(2) These rocks are calc-alkaline in nature, enriched in LREEs and LILEs, depleted in HREEs and HFSEs, and classified as sanukite.

(3) The primary magma of the high-Mg diorite was derived from partial melting of the depleted mantle wedge that had been metasomatized by subduction-related fluids, with insignificant crystallization fractionation.

(4) The magma was generated by moderate partial melting (20%–30%) of a garnet lherzolite source.

(5) The high-Mg diorite was formed by the northward subduction of the Paleo-Asian oceanic plate during the Middle Permian.

Author Contributions: Conceptualization, S.L. and Y.R.; formal analysis, S.L. and Q.Y.; investigation, S.L., Y.R., Q.Y., Y.H. and X.Z.; writing—original draft, S.L.; supervision, Y.R.; writing—review and editing, Y.R.; funding acquisition, Y.R. All authors have read and agreed to the published version of the manuscript.

Funding: This research was funded by the National Natural Science Foundation of China (NSFC), Grant/Award Number: 41772062.

Data Availability Statement: All data generated or used in the study are contained in the submitted article.

Acknowledgments: We are grateful to editors and reviewers for their constructive comments and significant help in improving the document and to the personnel assisting in field campaigns and laboratories.

Conflicts of Interest: The authors declare no conflict of interest.

References

1. Defant, M.J.; Drummond, M.S. Derivation of some modern arc magmas by melting of young subducted lithosphere. *Nature* **1990**, *347*, 662–665. [CrossRef]
2. Kamei, A.; Owada, M.; Nagao, T.; Shiraki, K. High-Mg diorites derived from sanukitic HMA magmas, Kyushu Island, southwest Japan arc: Evidence from clinopyroxene and whole rock compositions. *Lithos* **2004**, *75*, 359–371. [CrossRef]
3. Kay, R.W. Aleutian magnesian andesites: Melts from subducted Pacific Ocean crust. *J. Volcanol. Geoth. Res.* **1978**, *4*, 117–132. [CrossRef]
4. Rogers, G.; Saunders, A.D. Magnesian andesites from Mexico, Chile and the Aleutian Islands: Implications for magmatism associated with ridge-trench collision. In *Boninites and Related Rocks*; Crawford, A.J., Ed.; Unwin Hyman: London, UK, 1989; pp. 416–445.
5. Saunders, A.D.; Rogers, G.; Marriner, G.F.; Terrell, D.J.; Verma, S.P. Geochemistry of Cenezoic volcanic rocks, Baja California, Mexico: Implications for the petrogenesis of post-subduction magmas. *J. Volcanol. Geoth. Res.* **1987**, *32*, 223–245. [CrossRef]
6. Stern, J.A.; Hanson, G.A.; Shirey, S.B. Petrogenesis of mantle-derived, LILE-enriched Archean monzodiorites and trachyandesites (sanukitoids) in southwestern Superior Province. *Can. J. Earth Sci.* **1989**, *26*, 1688–1712. [CrossRef]
7. Tang, G.J.; Wang, Q. High-Mg andesites and their geodynamic implications. *Acta Petrol. Sin.* **2010**, *26*, 2495–2512, (In Chinese with English abstract).
8. Tatsumi, Y. Geochemical modeling of partial melting of subducting sediments and subsequent melt-mantle interaction: Generation of high-Mg andesites in the Setouchi volcanic belt, southwest Japan. *Geology* **2001**, *29*, 323–326. [CrossRef]
9. Bloomer, S.H.; Hawkins, J.W. Petrology and geochemistry of boninite series volcanic rocks from the Mariana trench. *Contrib. Mineral. Petrol.* **1987**, *97*, 361–377. [CrossRef]
10. Taylor, R.N.; Nesbitt, R.W.; Vidal, P.; Harmon, R.S.; Auvray, B.; Croudace, I.W. Mineralogy, chemistry, and genesis of the boninite series volcanics, Chichijima, Bonin-Islands, Japan. *J. Petrol.* **1994**, *35*, 577–617. [CrossRef]
11. Le bas, M.J. IUGS reclassification of the high-Mg and picritic volcanic rocks. *J. Petrol.* **2000**, *41*, 1467–1470. [CrossRef]
12. Martin, N.; Smithies, R.H.; Rapp, R.; Moyen, J.F.; Champion, D. An overview of adakite, mtonalite-trondhjemite-granodiorite (TTG), and sanukitoid: Relationships and some implications for crustal evolution. *Lithos* **2005**, *79*, 1–24. [CrossRef]
13. Xiao, W.J.; Windley, B.F.; Hao, J.; Zhai, M.G. Accretion leading to collision and the Permian Solonker suture, Inner Mongolia, China: Termination of the central Asian orogenic belt. *Tectonics* **2003**, *22*, 1–20. [CrossRef]
14. Zhang, Y.B.; Wu, F.Y.; Wilde, S.A.; Zhai, M.G.; Lu, X.P.; Sun, D.Y. Zircon U–Pb ages and tectonic implications of 'Early Paleozoic' granitoids at Yanbian, Jilin Province, Northeast China. *Isl. Arc* **2004**, *13*, 484–505. [CrossRef]
15. Sun, D.Y.; Wu, F.Y.; Zhang, Y.B.; Gao, S. The final closing time of the west Lamulun River-Changchun-Yanji plate suture zone: Evidence from the Dayushan granitic pluton, Jilin Province. *J. Jilin Univ. Earth Sci.* **2004**, *34*, 174–181, (In Chinese with English abstract).
16. Li, J.Y. Permian geodynamic setting of Northeast China and adjacent regions: Closure of the Paleo-Asian Ocean and subduction of the Paleo-Pacific Plate. *J. Asian Earth Sci.* **2006**, *26*, 207–224. [CrossRef]
17. Wu, F.Y.; Sun, D.Y.; Ge, W.C.; Zhang, Y.B.; Grant, M.L.; Wilde, S.A.; Jahn, B.M. Geochronology of the Phanerozoic granitoids in northeastern China. *J. Asian Earth Sci.* **2011**, *41*, 1–30. [CrossRef]
18. Cao, H.H.; Xu, W.L.; Pei, F.P.; Guo, P.Y.; Wang, F. Permian tectonic evolution of the eastern section of the northern margin of the North China Plate: Constraints from zircon U–Pb geochronology and geochemistry of the volcanic rocks. *Acta Petrol. Sin.* **2012**, *28*, 2733–2750, (In Chinese with English abstract).
19. Liu, Y.J.; Li, W.M.; Feng, Z.Q.; Wen, Q.B.; Neubauer, F.; Liang, C.Y. A review of the Paleozoic tectonics in the eastern part of Central Asian Orogenic Belt. *Gondwana Res.* **2017**, *43*, 123–148. [CrossRef]
20. Shao, J.A. *Crustal Evolution in the Middle Part of the Northern Margin of the Sino-Korean Plate*; Peking University Press: Beijing, China, 1991; pp. 1–136, (In Chinese with English abstract).
21. Xu, B.; Charvet, J.; Chen, Y.; Zhao, P.; Shi, G.Z. Middle Paleozoic convergent orogenic belts in western Inner Mongolia (China): Framework, kinematics, geochronology and implications for tectonic evolution of the Central Asian Orogenic Belt. *Gondwana Res.* **2013**, *23*, 1342–1364. [CrossRef]
22. Xu, B.; Zhao, P.; Wang, Y.Y.; Liao, W.; Luo, Z.W.; Bao, Q.Z.; Zhou, Y.H. The pre-Devonian tectonic framework of Xing'an-Mongolia orogenic belt (XMOB) in north China. *J. Asian Earth Sci.* **2015**, *97*, 183–196. [CrossRef]
23. Ren, Y.S.; Chen, C.; Zou, X.T.; Zhao, H.L.; Hao, Y.J.; Hou, H.N.; Hu, Z.C.; Jiang, G.H. The age, geological setting, and types of gold deposits in the Yanbian and adjacent areas, NE China. *Ore Geol. Rev.* **2016**, *73*, 284–297. [CrossRef]
24. Lu, S.Y.; Ren, Y.S.; Hao, Y.J.; Hou, H.N.; Yang, Q. Two-phase mineralization of Hongtaiping Cu polymetallic deposit in Yanbian area (NE China): Evidence from sulfide Rb-Sr dating and in-situ trace element analysis. *Ore Geol. Rev.* **2021**, *137*, 104295. [CrossRef]
25. Yu, J.J.; Men, L.J.; Chen, L.; Zhao, J.K.; Liang, S.N.; Chen, D.; Pang, W. SHRIMP U–Pb Ages of Zircon and Its Geological Implications from Metamorphic Dacite of the Wudaogou Group in Yanbian Area. *J. Jilin Univ. Earth Sci.* **2008**, *38*, 363–367, (In Chinese with English abstract).
26. Fu, C.L.; Sun, D.Y.; Zhang, X.Z.; Wei, H.Y.; Gou, J. Discovery and geological significance of the Triassic high-Mg diorites in Hunchun area, Jilin Province. *Acta Petrol. Sin.* **2010**, *26*, 1089–1102, (In Chinese with English abstract).

27. Liu, S.; Hu, R.Z.; Gao, S.; Feng, C.X.; Feng, G.Y.; Coulson, I.M.; Li, C.; Wang, T.; Qi, Y.Q. Zircon U–Pb age and Sr–Nd–Hf isotope geochemistry of Permian granodiorite and associated gabbro in the Songliao Block, NE China and implications for growth of juvenile crust. *Lithos* **2010**, *114*, 423–436. [CrossRef]
28. Guan, Q.B.; Li, S.C.; Zhang, C.; Shi, Y.; Li, P.C. Zircon U–Pb dating, geochemistry and geological significance of the I-type granites in Helong area, the eastern section of the southern margin of Xing-Meng Orogenic Belt. *Acta Petrol. Sin.* **2016**, *32*, 2690–2706, (In Chinese with English abstract).
29. Hou, H.N.; Ren, Y.S.; Lu, S.Y.; Hao, Y.J.; Yang, Q. Geodynamic setting of the south-east margin of Xing'an-Mongolian Orogenic Belt: Constraints from geochronology and geochemistry of the Permian volcanic rocks in Yanbian area, NE China. *Geol. J.* **2020**, *56*, 1258–1280. [CrossRef]
30. Tang, J.; Li, A.P.; Xu, W.L.; Liu, Y. Geochronology and geochemistry of late Carboniferous–Middle Jurassic magmatism in the Helong area, NE China: Implications for the tectonic transition from the Paleo-Asian oceanic to circum-Pacific regime. *Geol. J.* **2020**, *55*, 1808–1825. [CrossRef]
31. Zhao, Q.Y.; Li, C.F.; Li, D.C.; Chen, Y.J. Dating for zircons from gabbro dike of Wudaogou Group in Yanbian area and its geological significance. *Global Geol.* **2008**, *27*, 150–155, (In Chinese with English abstract).
32. Chen, Y.J.; Sun, J.G.; Ren, L.; Zhang, Y.; Men, L.J. Petrogenesis of the Wudaogou intermediate-mafic complex, NW China: Zircon U–Pb dating, whole-rock and isotope geochemistry, and geological implications. *Int. Geol. Rev.* **2015**, *55*, 1959–1977. [CrossRef]
33. Li, H.X.; Guo, F.; Li, C.W.; Zhao, L. Late Paleozoic subduction of the Paleo-Asian Ocean: Geochronological and geochemical records from Qianshan mafic intrusion in Hunchun area, NE China. *Acta Petrol. Sin.* **2010**, *26*, 1530–1540, (In Chinese with English abstract).
34. Cao, H.H.; Xu, W.L.; Pei, F.P.; Zhang, X.Z. Permian Tectonic Evolution in Southwestern Khanka Massif: Evidence from Zircon U–Pb Chronology, Hf isotope and Geochemistry of Gabbro and Diorite. *Acta Geol. Sin. Engl.* **2011**, *85*, 1390–1402.
35. Guo, F.; Li, H.X.; Fan, W.M.; Li, J.Y.; Zhao, L.; Huang, M.W. Variable sediment flux in generation of Permian subduction-related mafic intrusions from the Yanbian region, NE China. *Lithos* **2016**, *261*, 195–215. [CrossRef]
36. Safonova, I.Y.; Santosh, M. Accretionary complexes in the Asia-Pacific region: Tracing archives of ocean plate stratigraphy and tracking mantle plumes. *Gondwana Res.* **2014**, *25*, 126–158. [CrossRef]
37. Jahn, B.M.; Wu, F.Y.; Chen, B. Granitoids of the Central Asian Orogenic Belt and continental growth in the Phanerozoic. *Earth Environ. Sci. Trans. R. Soc. Edinb.* **2000**, *91*, 181–193.
38. Windley, B.F.; Alexeiev, D.; Xiao, W.J.; Kroener, A.; Badarch, G. Tectonic models for accretion of the Central Asian Orogenic Belt. *J. Geol. Soc.* **2007**, *164*, 31–47. [CrossRef]
39. Xiao, W.J.; Santosh, M. The western Central Asian Orogenic Belt: A window to accretionary orogenesis and continental growth. *Gondwana Res.* **2014**, *25*, 1429–1444. [CrossRef]
40. Sengör, A.M.C.; Natal'in, B.A.; Burtman, V.S. Evolution of the Altaid tectonic collage and Palaeozoic crustal growth in Eurasia. *Nature* **1993**, *364*, 299–307. [CrossRef]
41. Xu, W.L.; Sun, C.Y.; Tang, J.; Luan, J.P.; Wang, F. Basement nature and tectonic evolution of the Xing'an-Mongolian orogenic belt. *Earth Sci.* **2019**, *44*, 1620–1646, (In Chinese with English abstract).
42. Xu, W.L.; Wang, F.; Pei, F.P.; Meng, N.; Tang, J.; Xu, M.J.; Wang, W. Mesozoic tectonic regimes and regional ore-forming background in NE China: Constraints from spatial and temporal variations of Mesozoic volcanic rock associations. *Acta Petrol. Sin.* **2013**, *29*, 339–353, (In Chinese with English abstract).
43. Wu, F.Y.; Zhao, G.C.; Sun, D.Y.; Wilde, S.A.; Yang, J.H. The Hulan Group: Its role in the evolution of the Central Asian Orogenic Belt of NE China. *J. Asian Earth Sci.* **2007**, *30*, 542–556. [CrossRef]
44. Zhou, J.B.; Cao, J.L.; Wilde, S.A.; Zhao, G.C.; Zhang, J.J.; Wang, B. Paleo-Pacific Subduction–Accretion: Evidence from Geochemical and U–Pb Zircon Dating of the Nadanhada Accretionary Complex, NE China. *Tectonics* **2014**, *33*, 2444–2466. [CrossRef]
45. Bi, J.H.; Ge, W.C.; Yang, H.; Wang, Z.H.; Tian, D.X.; Liu, X.W.; Xu, W.L.; Xing, D.H. Geochemistry of MORB and OIB in the Yuejinshan Complex, NE China: Implications for Petrogenesis and Tectonic Setting. *J. Asian Earth Sci.* **2017**, *145*, 475–493. [CrossRef]
46. Jia, D.C.; Hu, R.Z.; Lu, Y.; Qiu, X.L. Collision belt between the Khanka block and the North China block in the Yanbian Region, Northeast China. *J. Asian Earth Sci.* **2004**, *23*, 211–219.
47. JBGMR (Jilin Bureau of Geology and Mineral Resources). *Regional Geology of Jilin Province*; Geological Publishing House: Beijing, China, 1988; (In Chinese with English abstract).
48. Wang, Z.G.; Wan, D.; Wang, K.Y.; Konare, Y.; Liang, Y.H. Isotope systematics and fluid inclusion studies of the Hongtaiping Cu–Pb–Zn deposit in Yanbian, NE China: Implications for ore genesis. *Geol. J.* **2020**, *55*, 6912–6935. [CrossRef]
49. Hou, H.N.; Ren, Y.S.; Lu, S.Y.; Hao, Y.J.; Yang, Q. Age and tectonic setting of vein-type mineralization of Hongtaiping copper polymetallic deposit in Yanbian area, Jilin Province, NE China. *Acta Petrol. Sin.* **2020**, *36*, 820–836, (In Chinese with English abstract).
50. Ma, Y.F.; Liu, Y.J.; Wang, Y.; Tang, Z.; Qian, C.; Qin, T.; Feng, Z.Q.; Sun, W.; Zang, Y.Q. Geochronology and geochemistry of the Carboniferous felsic rocks in the central Great Xing'an Range, NE China: Implications for the amalgamation history of Xing'an and Songliao–Xilinhot blocks. *Geol. J.* **2019**, *54*, 487–513. [CrossRef]
51. Zhang, C.; Neubauer, F.; Liu, Z.H.; Cui, F.H.; Guan, Q.B. Final-Stage Magmatic Record of Paleo-Asian Oceanic Subduction? Insights from Late Permian to Early Triassic Intrusive Rocks in the Yanbian Area, Easternmost Central Asian Orogenic Belt. *Minerals* **2020**, *10*, 799. [CrossRef]

52. Wiedenbeck, M.; Alle, P.; Corfu, M.; Griffin, W.L.; Meier, M.; Oberli, F.; Vonquadt, A.; Roddick, J.C.; Speigel, M. Three natural zircon standards for U–Th–Pb, Lu–Hf, trace element and REE analyses. *Geostand. Newsl.* **1995**, *19*, 1–23. [CrossRef]
53. Hao, Y.J.; Ren, Y.S.; Zhao, H.L.; Lai, K.; Zhao, X.; Ma, Y.P. Metallogenic Mechanism and Tectonic Setting of Tungsten Mineralization in the Yangbishan Deposit in Northeastern China. *Acta Geol. Sin. Engl.* **2018**, *92*, 241–267. [CrossRef]
54. Qi, L.; Zhou, M.F. Platinum-group elemental and Sr-Nd-Os isotopic geochemistry of Permian Emeishan flood basalts in Guizhou Province, SW China. *Chem. Geol.* **2008**, *248*, 83–103. [CrossRef]
55. Morel, M.L.A.; Nebel, O.; Nebel-Jacobsen, Y.J.; Miller, J.S.; Vroon, P.Z. Hafnium isotope characterization of the GJ-1 zircon reference material by solution and laser-ablation MC-ICPMS. *Chem. Geol.* **2008**, *255*, 231–235. [CrossRef]
56. Wu, F.Y.; Li, X.H.; Zheng, Y.F.; Gao, S. Lu–Hf isotopic systematics and their applications in petrology. *Acta Petrol. Sin.* **2007**, *23*, 185–220, (In Chinese with English abstract).
57. Blichert-Toft, J.; Albarede, F. The Lu–Hf isotope geochemistry of chongrites and the evolution of the mantle-crust system. *Earth Planet. Sci. Lett.* **1997**, *148*, 243–258. [CrossRef]
58. Nowell, G.M.; Kempton, P.D.; Noble, S.R.; Fitton, J.G.; Saunders, A.D.; Mahoney, J.J.; Taylor, R.N. High precision Hf isotope measurements of MORB and OIB by thermal ionisation mass spectrometry: Insights into the depleted mantle. *Chem. Geol.* **1998**, *149*, 211–233. [CrossRef]
59. Amelin, Y.; Lee, D.C.; Hallidat, A.N. Early-middle Archean crustal evolution deduced from Lu–Hf and U–Pb isotopic studies of single zircon grains. *Geochim. Cosmochim. Acta* **2000**, *64*, 4205–4225. [CrossRef]
60. Griffin, W.L.; Pearson, N.J.; Belousova, E.; Jackson, S.E.; van Achterbergh, E.; O'Reilly, S.Y.; Shee, S.R. The Hf isotope composition of cratonic mantle: LAM–MC–ICPMS analysis of zircon megacrysts in kimberlites. *Geochim. Cosmochim. Acta* **2000**, *64*, 133–147. [CrossRef]
61. Mahdy, N.M.; Ntaflos, T.; Pease, V.; Sami, M.; Slobodník, M.; Abu Steet, A.A.; Abdelfadil, K.M.; Fathy, D. Combined zircon U-Pb dating and chemical Th–U–total Pb chronology of monazite and thorite, Abu Diab A-type granite, Central Eastern Desert of Egypt: Constraints on the timing and magmatic-hydrothermal evolution of rare metal granitic magmatism in the Arabian Nubian Shield. *Geochemistry* **2020**, *80*, 125669.
62. Sun, S.S.; McDonough, W.F. Chemical and isotopic systematics of oceanic basalts: Implications for mantle composition and processes. *Geol. Soc.* **1989**, *42*, 313–345. [CrossRef]
63. Yang, J.; Wang, J.R.; Zhang, Q.; Chen, W.F.; Pan, Z.J.; Du, X.L.; Jiao, S.T.; Wang, S.H. Global IAB data excavation: The performance in basalt discrimination diagrams and preliminary interpretation. *Geol. B China* **2016**, *35*, 1937–1949, (In Chinese with English abstract).
64. Winchester, J.A.; Floyd, P.A. Geochemical discrimination of different magma series and their differentiation products using immobile elements. *Chem. Geol.* **1977**, *20*, 325–343. [CrossRef]
65. Hastie, A.R.; Kerr, A.C.; Pearce, J.A.; Mitchell, S.F. Classification of altered volcanic island arc rocks using immobile trace elements: Development of the Th–Co discrimination diagram. *J. Petrol.* **2007**, *48*, 2341–2357. [CrossRef]
66. Yang, J.H.; Wu, F.Y.; Shao, J.A.; Wilde, S.A.; Xie, L.W.; Liu, X.M. Constraints on the timing of uplift of the Yanshan Fold and Thrust Belt, North China. *Earth Planet. Sci. Lett.* **2006**, *246*, 336–352. [CrossRef]
67. Koschek, G. Origin and significance of the SEM cathodoluminescence from zircon. *J. Microsc.* **1993**, *171*, 223–232. [CrossRef]
68. Belousova, E.; Griffin, W.; O'Reilly, S.Y.; Fisher, N. Igneous zircon: Trace element composition as an indicator of source rock type. *Contrib. Mineral. Petrol.* **2002**, *143*, 602–622. [CrossRef]
69. Cao, H.H.; Xu, W.L.; Pei, F.P.; Wang, Z.W.; Wang, F.; Wang, Z.J. Zircon U–Pb geochronology and petrogenesis of the Late Paleozoic-Early Mesozoic intrusive rocks in the eastern segment of the northern margin of the North China Block. *Lithos* **2013**, *170*, 191–207. [CrossRef]
70. Men, L.J. An Ore-Forming Fluid Study on Late Mesozoic Epithermal Au-Cu Deposits in Yanbian-Dongning Area: Implication for the Metallogenic Mechanism. Ph.D. Thesis, Jilin University, Changchun, China, 2011. (In Chinese with English abstract).
71. Ju, N. Ore Genesis and Tectonic Settings of Lishan Polymetallic Deposit in Tianbaoshan Metallogenic Region, Yanbian Area. Master's Thesis, Jilin University, Changchun, China, 2013. (In Chinese with English abstract).
72. Sun, Z.M.; Ren, Y.S.; Ju, N.; Zhao, H.L.; Chen, C.; Sun, Y.C. Superimposed mineralization of the Tianbaoshan metallogenic region in Yanbian area (eastern Jilin Province), northeastern China: Indicated by the isotopic dating. *Acta Petrol. Sin.* **2014**, *30*, 2081–2091, (In Chinese with English abstract).
73. Yang, Q.; Ren, Y.S.; Ju, N.; Zhang, B.; Chen, C.; Sun, Z.M. Geochronology and geochemistry of the metallogenic intrusion in the Xinxing lead-zinc (silver) deposit in the Tianbaoshan ore concentration area, Yanbian Prefecture. *Acta Petrol. Mineral.* **2015**, *34*, 295–308, (In Chinese with English abstract).
74. Yang, Q.; Ren, Y.S.; Sun, Z.M.; Hao, Y.J.; Zhang, B.; Sun, X.H.; Lu, S.Y. Geochronologic evidence of Late Paleozoic magmatic-hydrothermal mineralization in Tianbaoshan metallogenic region, Yanbian area: A case study of the Xinxing lead-zinc (silver) deposit. *Acta Petrol. Sin.* **2018**, *34*, 3153–3166, (In Chinese with English abstract).
75. Zhang, Y.; Xing, S.W.; Zhang, Z.J.; Ma, Y.B.; Wang, Y.; Ding, J.H.; Yu, Z.T.; Li, C.; Zhang, B. Genesis of the Tianbaoshan Polymetallic Ore District, Yanbian, NE China: Constraints from Geochronology and Isotopic Analysis. *Resour. Geol.* **2017**, *67*, 300–315. [CrossRef]
76. Polat, A.; Hofmann, A.W.; Rosing, M.T. Boninite-like volcanic rocks in the 3.7–3.8 Ga Isua greenstone belt, West Greenland: Geochemical evidence for intra-oceanic subduction zone processes in the early Earth. *Chem. Geol.* **2002**, *184*, 231–254. [CrossRef]

77. Liu, S.; Hu, R.Z.; Gao, S.; Feng, C.X.; Qi, L.; Zhong, H.; Xiao, T.F.; Qi, Y.Q.; Wang, T.; Coulson, I.M. Zircon U–Pb geochronology and major, trace elemental and Sr–Nd–Pb isotopic geochemistry of mafic dykes in western Shandong Province, east China: Constrains on their petrogenesis and geodynamic significance. *Chem. Geol.* **2008**, *255*, 329–345. [CrossRef]
78. Spera, F.J.; Bohrson, W.A. Energy-Constrained Open-System Magmatic Processes I: General Model and Energy-Constrained Assimilation and Fractional Crystallization (EC-AFC) Formulation. *J. Petrol.* **2001**, *42*, 999–1018. [CrossRef]
79. Rudnick, R.L.; Gao, S. Composition of the continental crust. *Treatise Geochem.* **2003**, *3*, 1–64.
80. Taylor, S.R.; McLennan, S.M. *The Continental Crust: Its Composition and Evolution: An Examination of the Geochemical Record Preserved in Sedimentary Rocks*; Blackwell Scientific: Oxford, UK, 1985.
81. Fitton, J.G.; James, D.; Kempton, P.D.; Ormerod, D.S.; Leeman, W.P. The role of lithospheric mantle in the generation of late Cenozoic basic magmas in the western United States. *J. Petrol.* **1988**, *1*, 331–349. [CrossRef]
82. Thompson, R.N.; Morrison, M.A. Asthenospheric andlower-lithospheric mantle contributions to continental extensional magmatism: An example from the British Tertiary Province. *Chem. Geol.* **1988**, *68*, 1–15. [CrossRef]
83. McCulloch, M.T.; Gamble, J.A. Geochemical and geodynamicai constraints on subduction zone magmatism. *Earth Planet. Sci. Lett.* **1991**, *102*, 358–374. [CrossRef]
84. Ridolfi, F.; Renzulli, A.; Puerini, M. Stability and chemical equilibrium of amphibole in calc-alkaline magmas: An overview, new thermobarometric formulations and application to subduction-related volcanoes. *Contrib. Mineral. Petrol.* **2010**, *160*, 45–66. [CrossRef]
85. Botcharnikov, R.E.; Almeev, R.R.; Koepke, J.; Holtz, F. Phase Relations and Liquid Lines of Descent in Hydrous Ferrobasalt—Implications for the Skaergaard Intrusion and Columbia River Flood Basalts. *J. Petrol.* **2008**, *49*, 1687–1727. [CrossRef]
86. Feng, G.Y.; Liu, S.; Feng, C.X.; Jia, D.C.; Zhong, H.; Yu, X.F.; Qi, Y.Q.; Wang, T. Zircon U–Pb age, Sr–Nd–Hf isotope geochemistry and the petrogenesis of the ultramafic pluton in Hongqiling, Jilin Province. *Acta Petrol. Sin.* **2011**, *27*, 1594–1606, (In Chinese with English abstract).
87. Johnson, K.T.M. Experimental determination of partition coefficients for rare earth and high-field-strength elements between clinopyroxene, garnet, and basaltic melt at high pressures. *Contrib. Mineral. Petr.* **1998**, *133*, 60–68. [CrossRef]
88. McKenzie, D.P.; O'Nions, R.K. Partial Melt Distributions from Inversion of Rare Earth Element Concentrations. *J. Petrol.* **1991**, *32*, 1021–1091. [CrossRef]
89. Yang, Q.; Ren, Y.S.; Hao, Y.J.; Wang, B.; Sun, Z.M.; Li, J.M. Ore fluid, geochronology and tectonic setting of mesothermal gold metallogeny in southeastern Jilin Province, Northeast China: A case study of the Shajingou gold deposit. *Ore Geol. Rev.* **2019**, *109*, 229–252. [CrossRef]
90. Hanyu, T.; Tatsumi, Y.; Nakai, S.; Chang, Q.; Miyazaki, T.; Sato, K.; Tani, K.; Shibata, T.; Yoshida, T. Contribution of slab melting and slab dehydration to magmatism in the NE Japan arc for the last 25Myr: Constraints from geochemistry. *Geochem. Geophys. Geosyst.* **2006**, *7*, 1–29. [CrossRef]
91. Pearce, J.A.; Peate, D.W. Tectonic Implications of the Composition of Volcanic Arc Magmas. *Annu. Rev. Earth Plant. Sci.* **1995**, *23*, 251–285. [CrossRef]
92. Wu, F.Y.; Zhang, X.Z.; Ma, Z.H.; Sun, D.Y. Piemontite-bearing chert in central Jilin: Characterization and implication. *Geol. B China* **2003**, *22*, 391–396, (In Chinese with English abstract).
93. Li, C.D.; Zhang, F.Q.; Miao, L.C.; Xie, H.Q.; Xu, Y.W. Zircon SHRIMP geochronology and geochemistry of Late Permian high-Mg andesites in Seluohe area, Jilin Province, China. *Acta Petrol. Sin.* **2007**, *23*, 767–776, (In Chinese with English abstract).
94. Yu, Q.; Ge, W.C.; Yang, H.; Zhao, G.C.; Zhang, Y.L.; Su, L. Petrogenesis of late Paleozoic volcanic rocks from the Daheshen Formation in Central Jilin Province, NE China, and its tectonic implications: Constraints from geochronology, geochemistry and Sr–Nd–Hf Isotopes. *Lithos* **2014**, *192–195*, 116–131. [CrossRef]
95. Song, Z.G.; Han, Z.Z.; Gao, L.H.; Geng, H.Y.; Li, X.P.; Meng, F.X.; Han, M.; Zhong, W.J.; Li, J.J.; Du, Q.X.; et al. Permo-Triassic evolution of the southern margin of the Central Asian Orogenic Belt revisited: Insights from Late Permian igneous suite in the Daheishan Horst, NE China. *Gondwana Res.* **2018**, *56*, 23–50. [CrossRef]
96. Bailey, J.C. Geochemical criteria for a refined tectonic discrimination of orogenic andesites. *Chem. Geol.* **1981**, *32*, 139–154. [CrossRef]
97. Pearce, J.A. Role of the sub-continental lithosphere in magma genesis at active continental margins. In *Continental Basalts and Mantle Xenoliths*; Hawkesworth, C.J., Norry, M.J., Eds.; Shiva Publications: Nantwich, UK, 1983; pp. 230–249.
98. Shen, Y.J.; Chen, B.; Li, J.Y.; Sun, J.L.; Zhao, C.J.; Zheng, T.; Liu, J.L. Geochemical characteristics, petrogenesis and geological significance of early Triassic high magnesium diorite in central Jilin province. *J. Heilongjiang Univ. Sci. Tech.* **2020**, *30*, 481–489, (In Chinese with English abstract).
99. Yuan, L.L.; Zhang, X.H.; Xue, F.H.; Lu, Y.H.; Zong, K.Q. Late Permian high-Mg andesite and basalt association from northern Liaoning, North China: Insights into the final closure of the Paleo-Asian ocean and the orogen–craton boundary. *Lithos* **2016**, *258*, 58–76. [CrossRef]
100. Jing, Y.; Ge, W.C.; Dong, Y.; Yang, H.; Ji, Z.; Bi, J.H.; Zhou, H.Y.; Xing, D.H. Early–Middle Permian southward subduction of the eastern Paleo-Asian Ocean: Constraints from geochronology and geochemistry of intermediate-acidic volcanic rocks in the northern margin of the North China Craton. *Lithos* **2020**, *364–365*, 105491. [CrossRef]